RSC Advances

PAPER

View Article Online
View Journal | View Issue

Cite this: *RSC Adv.*, 2018, **8**, 6988

Photocatalytic activity of $BiFeO_3/ZnFe_2O_4$ nanocomposites under visible light irradiation†

B. Safizade, S. M. Masoudpanah,* M. Hasheminiasari and A. Ghasemi

Received 16th December 2017
Accepted 31st January 2018

DOI: 10.1039/c7ra13380d

rsc.li/rsc-advances

Herein, $BiFeO_3/ZnFe_2O_4$ nanocomposites were synthesized *via* a glyoxylate precursor method using a two-pot approach. Phase evolution is investigated by X-ray diffraction and Raman spectroscopy, which confirm that no impurity phases are formed between $BiFeO_3$ and $ZnFe_2O_4$ following calcination at 600 °C. The specific surface area characterized by N_2 adsorption–desorption isotherms decreases from 30.56 to 13.13 $m^2\ g^{-1}$ with the addition of zinc ferrite. In contrast, the magnetization increases from 0.28 to 1.8 emu g^{-1} with an increase in the amount of $ZnFe_2O_4$. The composites show strong absorption in the visible region with the optical band gap calculated from the Tauc's plot in the range from 2.17 to 2.22 eV, as measured by diffuse reflectance spectroscopy. Furthermore, the maximum efficiency for the photodegradation of methylene blue under visible light is displayed by the composite containing 25 wt% $ZnFe_2O_4$ due to the synergic effect between $BiFeO_3$ and $ZnFe_2O_4$, as confirmed by photoluminescence spectroscopy.

1. Introduction

In recent years, scientific research has been focused on new visible light photocatalysts based on semiconductors to address the increasing environmental pollution and energy demands by efficient utilization of solar energy.[1,2] To date, various metal oxides (ZnO[3] and TiO_2 [4]) and metal sulfides (ZnS[5]) have been studied to efficiently degrade harmful organic pollutants and for hydrogen production through water splitting under UV light irradiation.[4] However, the UV region spans only 5% of the entire solar spectrum, restricting their applications. As a result of band gap engineering improvement, composites can be fabricated by coupling two narrow band gap semiconductors, which have attracted considerable attention for the development of efficient visible light photocatalysts.[6–8]

Bismuth ferrite ($BiFeO_3$), which has potential applications in sensors, actuators, and digital memory, is a well-known multiferroic material simultaneously possessing ferroelectric and ferromagnetic ordering at room temperature.[9,10] Furthermore, $BiFeO_3$ displays a distinct photovoltaic effect with an open circuit voltage of 0.8–0.9 V as a working solar device, which represents a new potential application.[11,12] Due to its relatively narrow band gap of 2.2 eV, $BiFeO_3$ has been considered as a possible visible light photocatalyst under solar light irradiation for the photodegradation of organic contaminants.[13,14] However, its quantum yield is poor due to the rapid recombination of the photogenerated electron–hole pairs that limits its practical use in photocatalytic applications.[15,16] Therefore, many strategies have been developed to enhance the photocatalytic efficiency of $BiFeO_3$ by modifying the size and morphology of its particles, cation doping, and coupling with other semiconductors.[17–19] For instance, several semiconductors such as g-C_3N_4, carbon nanofiber, graphene, CuO and ZnO have been coupled with $BiFeO_3$ to improve its photogenerated electron–hole separation, thus enhancing its interfacial charge transfer the efficiency.[6,20–27]

Spinel magnetic zinc ferrite ($ZnFe_2O_4$) with a narrow band gap of 1.92 eV exhibits a significant photoresponse in the visible light region and has been utilized in gas sensors, catalysts and semiconductor photocatalysts.[1] Furthermore, the magnetic properties of $ZnFe_2O_4$ can be used to recycle photocatalysts by the application of a magnetic field, making it an interesting product in the industrial photodegradation of organic pollutants.[7,28] To the best of our knowledge, there are no reports on the synthesis and application of $BiFeO_3/ZnFe_2O_4$ nanocomposites for pollutant degradation under visible light irradiation. Uniyal and Yadav only reported the dielectric and magnetic properties of $BiFeO_3/ZnFe_2O_4$ composites synthesized *via* the sol–gel method as a function of annealing temperature.[29]

Herein, we report the structure, microstructure, magnetic properties and photocatalytic performances of $BiFeO_3/ZnFe_2O_4$ composites synthesized *via* the glyoxylate precursor method. The optimum amount of $ZnFe_2O_4$ is determined to maximize the photocatalytic activity of $BiFeO_3$ powder.

2. Experimental procedure

Starting materials of $Fe(NO_3)_3\cdot 9H_2O$ (>99%), $Bi(NO_3)_2\cdot 5H_2O$ (>99%), $Zn(NO_3)_2\cdot 6H_2O$ (>99%), 1,2-ethanediol ($OH(CH_2)_2OH$)

School of Metallurgy & Materials Engineering, Iran University of Science and Technology (IUST), Tehran, Iran. E-mail: masoodpanah@iust.ac.ir; Fax: +98 21 77240480; Tel: +98 21 77240540

† Electronic supplementary information (ESI) available: The UV-vis spectra and refined XRD patterns. See DOI: 10.1039/c7ra13380d

and nitric acid (HNO_3, 68 wt%) of analytical grade were provided by Merck & Co.

$BiFeO_3$ powder was prepared *via* the glyoxylate precursor method in which the required amount of $Fe(NO_3)_3 \cdot 9H_2O$ was dissolved in 1,2-ethanediol (ethylene glycol) and then added to 15 mL of 3 mol L^{-1} nitric acid solution containing $Bi(NO_3)_3 \cdot 5H_2O$ under magnetic stirring at 100 °C. The ethylene glycol : NO_3^- (EG/NO_3) molar ratio was set to 2.5 : 1. Evolving bubbles of brown nitrogen oxide (NO_x) indicated the initiation of the redox reaction between the NO_3^- anions and OH groups of diol. After drying at 130 °C, the precursor was calcined at 600 °C for 1 h in ambient air.[30] $ZnFe_2O_4$ powder was produced by dissolving $Zn(NO_3)_2 \cdot 6H_2O$ and $Fe(NO_3)_3 \cdot 9H_2O$ in ethylene glycol under magnetic stirring at 100 °C. Once the NO_x bubbles disappeared, the solution precursor was dried at 130 °C and then calcined at 600 °C for 1 h in air. $BiFeO_3/ZnFe_2O_4$ composites were synthesized *via* a two-pot approach in which the required amount of previously synthesized $BiFeO_3$ powder was added to the solution precursor of zinc ferrite, where the dried precursor was calcined at 600 °C for 1 hour.

Phase evolution was investigated using a PANalytical X'pert X-ray diffractometer (XRD) with monochromatic CuKα radiation. Raman analysis was performed on the powders using a WiTec Alpha 300R instrument (Nd:YAG laser source: λ = 532 nm and 0.7 MW power, and range: 100–900 cm^{-1}). The morphology and microstructure of the powders were observed using a TESCAN Vega II scanning electron microscope (SEM). The specific surface areas of the as-prepared powders were determined according to the Brunauer–Emmett–Teller (BET) method with nitrogen adsorption at 77 K using a PHS-1020 instrument after degassing at 250 °C for 5 h. The Barrett–Joyner–Halenda (BJH) cumulative pore volume was calculated from the adsorption branch of the isotherms. The equivalent particle size was calculated based on the BET surface area as follows:

$$D_{BET} = \frac{6000}{\rho S_{BET}} \quad (1)$$

where, D_{BET} is the equivalent particle size (nm), ρ is the theoretical density and S_{BET} stands for the BET surface area ($m^2\ g^{-1}$). A vibrating sample magnetometer (Meghnatis Daghigh Kavir Kashan Co., Iran) with a maximum field of 10 kOe was employed to measure the magnetic properties at room temperature. UV-vis absorption spectra were recorded on a Shimadzu UV-vis-52550 spectrophotometer in the wavelength range of 300−800 nm. Room temperature photoluminescence spectra (PL) were obtained on a fluorescence spectrophotometer (F-4600, Hitachi, Japan) at an excitation wavelength of 210 nm.

The photocatalytic activity of the $BiFeO_3/ZnFe_2O_4$ nanocomposites was evaluated by the degradation of methylene blue (MB) in aqueous solution under visible light radiation. Two 100 W xenon lamps with a cutoff ultraviolet filter (λ = 420 nm) were introduced as the visible light source. In each experiment, 0.1 g of photocatalyst was added to 100 mL of methylene blue solution at a concentration of 15 mg L^{-1}. In addition, the solution pH was adjusted to 2 by adding HCl to obtain the maximum MB adsorption on the catalyst surface,[14] as shown in the ESI.† The suspension was stirred in the dark for 60 min to establish the adsorption/desorption equilibrium, then the solution was irradiated under visible light. At appropriate time intervals, about 5 mL of suspension was sampled, where the solid phase was separated from the solution *via* centrifugation at 4000 rpm for 20 min. The concentration of each degraded solution was monitored on a PG Instruments Ltd T80-UV/vis spectrophotometer.

3. Results and discussion

Fig. 1 shows the XRD patterns of the pure $BiFeO_3$, pure $ZnFe_2O_4$ and the $BiFeO_3$–$x$$ZnFe_2O_4$ composites. The indexed diffraction peaks of $ZnFe_2O_4$ are (220), (311), (400), (422), (511), (440) and (533) which match well with the cubic spinel structure having the $Fd\bar{3}m$ space group and are in good agreement with the standard JCPDS card no. 22-1012. Pure $BiFeO_3$ shows indexed diffraction peaks corresponding to a rhombohedral phase with the $R3c$ space group (JCPDS no. 86-1518), which indicates well crystallized $BiFeO_3$ nanoparticles were produced by the glyoxylate precursor method. However, some impurity $Bi_2Fe_4O_9$ phases (JCPDS card no. 42-0181) were also observed with $BiFeO_3$. The chemical synthesis of $BiFeO_3$ typically leads to the formation of impurities, may be due to its chemical kinetics.[31] After compositing with 25 wt% $ZnFe_2O_4$, a weak diffraction peak at $2\theta = 35.32°$ corresponding to the (311) reflection peak of $ZnFe_2O_4$ appeared. With an increase in the zinc ferrite content, the diffraction peaks of $ZnFe_2O_4$ became clearer and stronger, and the impurity peak disappeared. Furthermore, no impurity species were formed between $BiFeO_3$ and $ZnFe_2O_4$ during the calcination process, which indicates that $ZnFe_2O_4$ was successfully loaded on the $BiFeO_3$ particles without destroying its crystal structure. The amount of $BiFeO_3$ and $ZnFe_2O_4$ phases

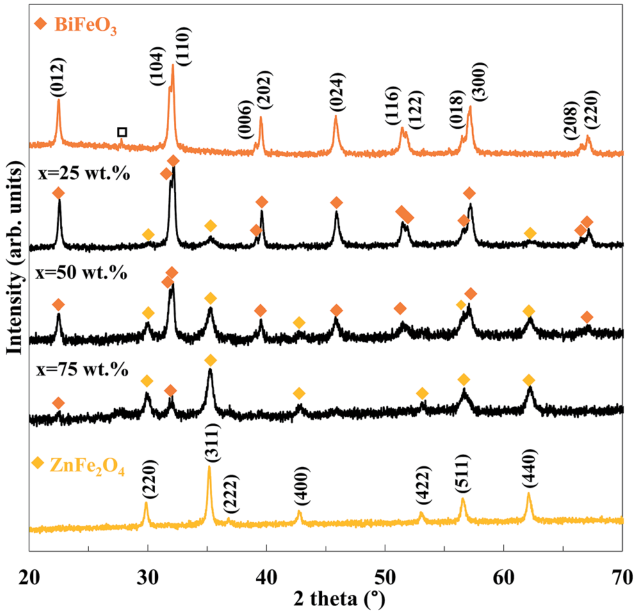

Fig. 1 XRD patterns of the $BiFeO_3$–$x$$ZnFe_2O_4$ composites as a function of $ZnFe_2O_4$ content (x) ($Bi_2Fe_4O_9$).

in the composites was calculated by Rietveld refinement, which is in agreement with the nominal values, as typically shown in the ESI.†

The Raman spectra of pure $BiFeO_3$, pure $ZnFe_2O_4$ and $BiFeO_3$–$x$$ZnFe_2O_4$ composites are presented in Fig. 2. In the spectrum of pure $BiFeO_3$, the Raman active modes with A_1 and E symmetry can be summarized using the following irreducible representation $\Gamma = 4A_1 + 9E$.[32] The two peaks at 173 and 220 cm^{-1} are assigned as A1 modes, and the peaks at 286, 361 and 481 cm^{-1} correspond to the E modes. Pure $ZnFe_2O_4$ exhibited four peaks at 246, 327, 471 and 648 cm^{-1}, which are assigned as the $T_{2g}(1)$, E_g, $T_{2g}(2)$ and A_{1g} modes for a cubic spinel structure, respectively.[33] The A_{1g} mode of $ZnFe_2O_4$ appears after 25 wt% $ZnFe_2O_4$ was loaded, while the other modes were dominant at higher zinc ferrite contents. Moreover, the purity of the $BiFeO_3$–$x$$ZnFe_2O_4$ composites is confirmed by the absence of Raman modes of impurity phases.

The SEM images of pure $BiFeO_3$, $BiFeO_3$-25 wt% $ZnFe_2O_4$, $BiFeO_3$-75 wt% $ZnFe_2O_4$ and pure $ZnFe_2O_4$ powders are displayed in Fig. 3. The quasi-spherical particles of $BiFeO_3$ (210 nm) are larger than the $ZnFe_2O_4$ particles (80 nm). However, the $BiFeO_3$-25 wt% $ZnFe_2O_4$ composite is composed of plate-like particles. Furthermore, the average particle size decreases while the particle size distribution becomes rather uniform with an increase in $ZnFe_2O_4$ content.

The N_2 adsorption–desorption isotherms of the $BiFeO_3$-50 wt% $ZnFe_2O_4$ composite are shown in Fig. 4. Table 1 also presents the specific surface area (S_{BET}), equivalent particle size (D_{BET}) and pore volume. The particle agglomerations show a typical type II isotherm according to the International Union of Pure and Applied Chemistry (IUPAC) classification.[34] The surface area of pure $BiFeO_3$ is 30.56 $m^2\ g^{-1}$ and 13.13 $m^2\ g^{-1}$ for pure $ZnFe_2O_4$. The higher specific surface area of pure $BiFeO_3$ is attributed to more gaseous products being formed during its synthesis,[35] as confirmed by its higher pore volume (0.089 $cm^3\ g^{-1}$). The BJH pore size distribution is also depicted in the inset of Fig. 4. The pore size distribution of the $BiFeO_3$-50 wt% $ZnFe_2O_4$ composite powder exhibits a mesopore spreading of about 3–4 nm.

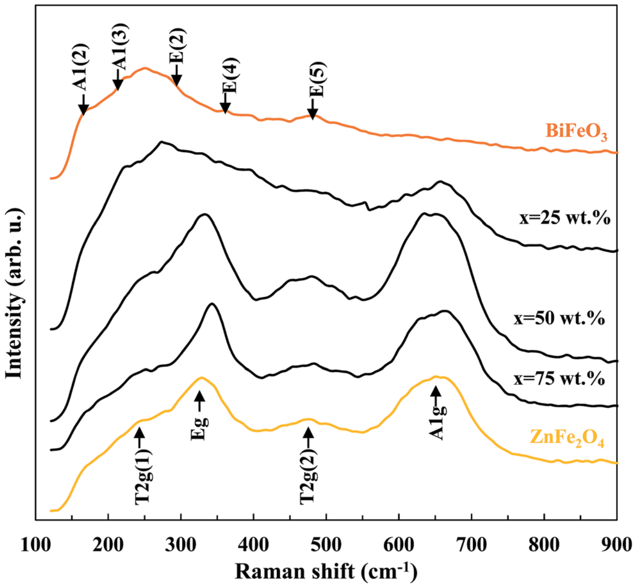

Fig. 2 Raman spectra of the $BiFeO_3$–$x$$ZnFe_2O_4$ composites.

Fig. 5 illustrates the magnetization curves of the $BiFeO_3$–$x$$ZnFe_2O_4$ composites as well as the pure $BiFeO_3$ and $ZnFe_2O_4$ powders. The pure $BiFeO_3$ nanoparticles exhibit a ferrimagnetic response with the magnetization of 0.28 emu g^{-1} at 10 kOe. However, the magnetization increases with an increase in zinc ferrite content since pure $ZnFe_2O_4$ has a magnetization of 1.8 emu g^{-1}. Bulk $BiFeO_3$ is known to show a G-type antiferromagnetic ordering with a linear field-dependence of magnetization, while the $BiFeO_3$ nanoparticles exhibit weak ferrimagnetism due to the interruption of the long-range antiferromagnetic order at the particle surface.[36] The bulk $ZnFe_2O_4$ also has a normal spinel structure with antiferromagnetic behavior, while the $ZnFe_2O_4$ nanoparticles exhibit a partially inverse spinel structure with some magnetic moment at room temperature.[37] A high surface-to-volume ratio in nanoparticles leads to more uncompensated spins from the surface, inducing an enhancement in magnetization. The $BiFeO_3$–$x$$ZnFe_2O_4$ composites show higher saturation magnetization than pure bismuth ferrite as a result of the higher magnetization in the zinc ferrite phase. This ferrimagnetism behavior can be exploited for the magnetic recovery of the photocatalyst after degradation.

The optical properties of the $BiFeO_3$–$x$$ZnFe_2O_4$ composites, as well as the pure $BiFeO_3$ and $ZnFe_2O_4$ powders were investigated *via* UV-vis diffuse reflectance spectroscopy, which are presented in Fig. 6. The absorption spectra show that the samples absorb a considerable amount of visible light. The direct optical band gap, E_g, was determined using the equation $(\alpha h\nu)^2 = A(h\nu - E_g)$, where, $h\nu$ is the photon energy in eV, α is the absorption coefficient and A is a material constant,[38] as shown in the inset of Fig. 6. According to the Tauc plots, the band gaps for $x = 0$, 25, 50, 75 and 100 wt% were calculated to be 2.17, 2.03, 2.14, 2.15 and 2.22 eV, respectively. The absorption band of $BiFeO_3$ and $ZnFe_2O_4$ is attributed to the electronic transition from the valence band (O 2p orbital) to the conduction band (Fe 3d orbital) ($O_{2p}{}^{2-} \rightarrow Fe_{3d}{}^{3+}$).[39,40] Clearly, the band gap of the $BiFeO_3$–$x$$ZnFe_2O_4$ photocatalysts gradually decreases with an increase in $BiFeO_3$. In other words, by introducing $ZnFe_2O_4$ into $BiFeO_3$, the photocatalyst could absorb more visible light for the production of electron–hole pairs, which are favorable for photocatalytic reactions.

Fig. 7a shows the UV-vis spectra of the MB solution after different irradiation times in the presence of the $BiFeO_3$-25 wt% $ZnFe_2O_4$ composite. The main absorption peaks of MB molecules at 664 nm almost completely disappeared after about 120 min, which suggests the excellent photocatalytic activity of the $BiFeO_3$-25 wt% $ZnFe_2O_4$ composite. The photodegradation efficiency of MB dye by pure $BiFeO_3$, pure $ZnFe_2O_4$ and $BiFeO_3$–$x$$ZnFe_2O_4$ composites as a function of irradiation time are summarized in Fig. 7b.

Methylene blue was hardly degraded (∼3%) by pure $ZnFe_2O_4$ which exhibited very limited photolysis of MB under visible light irradiation. The low photocatalytic efficiency of pure

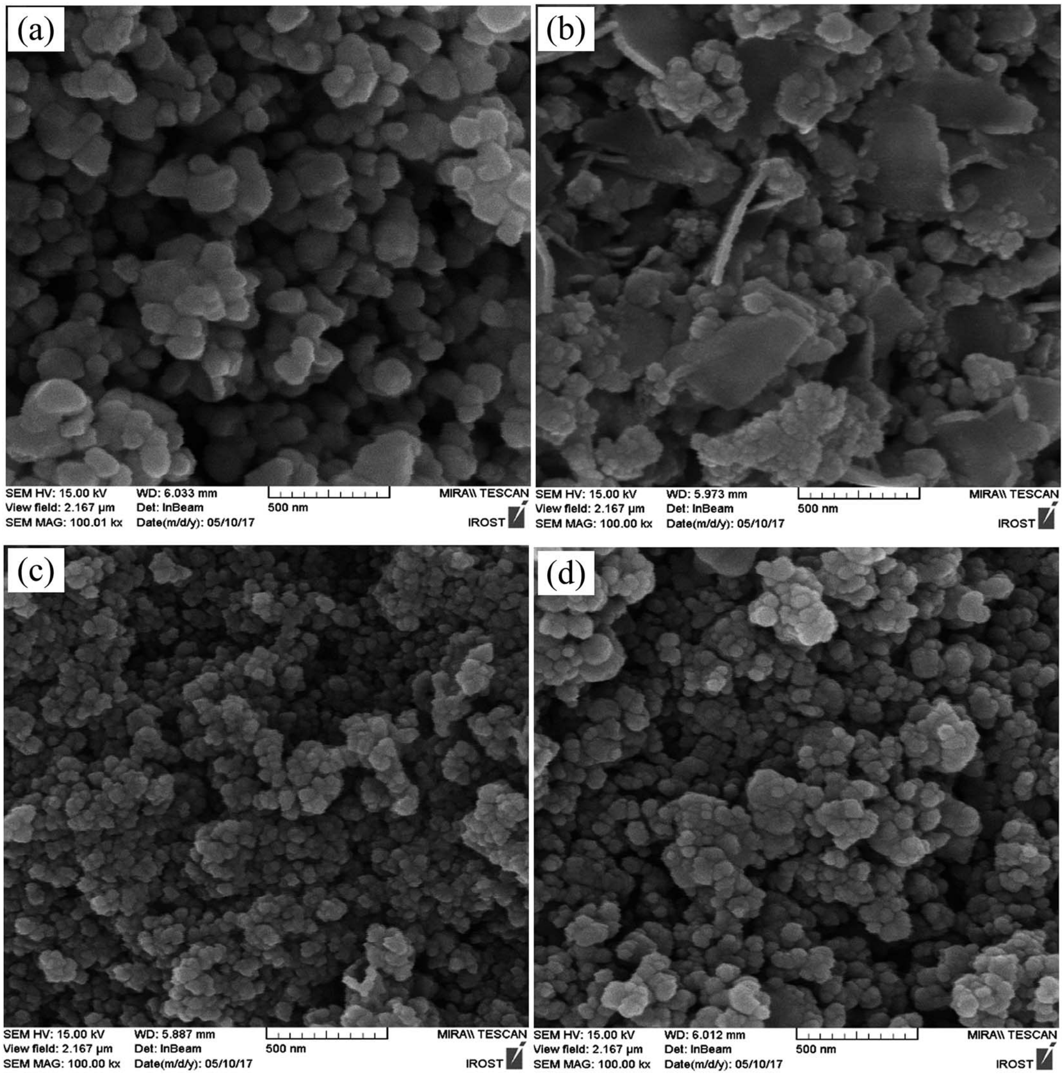

Fig. 3 SEM images of (a) pure $BiFeO_3$, (b) $BiFeO_3$-25 wt% $ZnFe_2O_4$, (c) $BiFeO_3$-75 wt% $ZnFe_2O_4$, and (d) pure $ZnFe_2O_4$ powders.

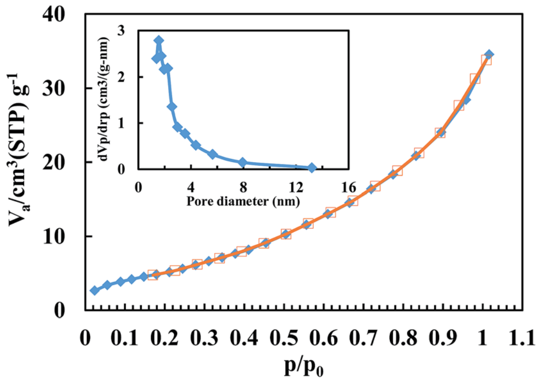

Fig. 4 Adsorption (filled symbol)–desorption (open symbol) isotherms of the $BiFeO_3$-50 wt% $ZnFe_2O_4$ composite (the inset shows the pore size distribution).

Table 1 Dependence of specific surface area, S_{BET}, pore volume and equivalent particle size, D_{BET}, on $ZnFe_2O_4$ content (x)

x	S_{BET} (m^2 g^{-1})	Pore volume (cm^3 g^{-1})	D_{BET} (nm)
$BiFeO_3$	30.56	0.089	23.6
25 wt%	28.42	0.086	27.9
50 wt%	19.75	0.072	44.8
75 wt%	18.97	0.069	52.6
$ZnFe_2O_4$	13.13	0.053	87.1

$ZnFe_2O_4$ can be attributed to its low valence band potential and poor photoelectric conversion.[7,41] However, pure $BiFeO_3$ can degrade 94.5% of MB after 2 hours of irradiation. The maximum MB photodegradation of ~97% was observed for the $BiFeO_3$-25 wt% $ZnFe_2O_4$ composite after 30 minutes of irradiation. The extraordinary photocatalytic efficiency of the $BiFeO_3$-25 wt% $ZnFe_2O_4$ composite may be attributed to the formation of $BiFeO_3$–$ZnFe_2O_4$ heterojunctions, which promote the separation of photogenerated electron–hole pairs, thus enhancing the photocatalytic activity. However, the number of effective heterojunctions and thus separation efficiency strongly depend

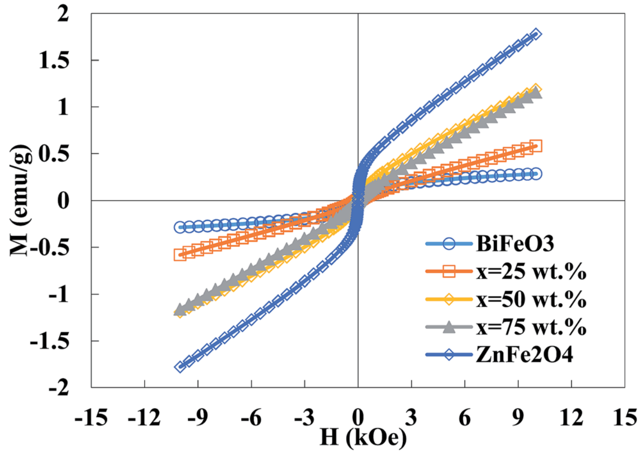

Fig. 5 Magnetization curves of the $BiFeO_3$–$xZnFe_2O_4$ composites.

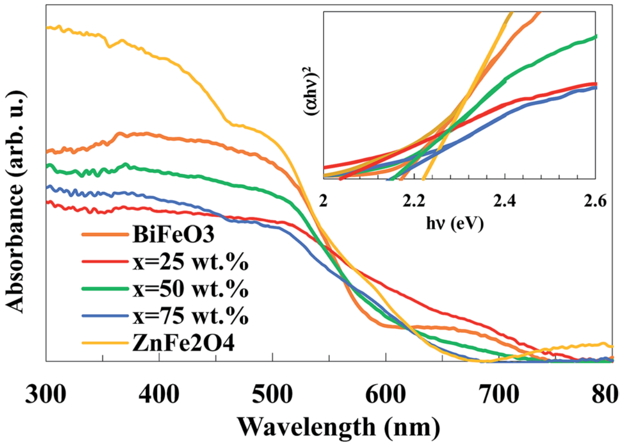

Fig. 6 UV-vis absorption spectra of the $BiFeO_3$–$xZnFe_2O_4$ composites (the inset shows the Tauc plots).

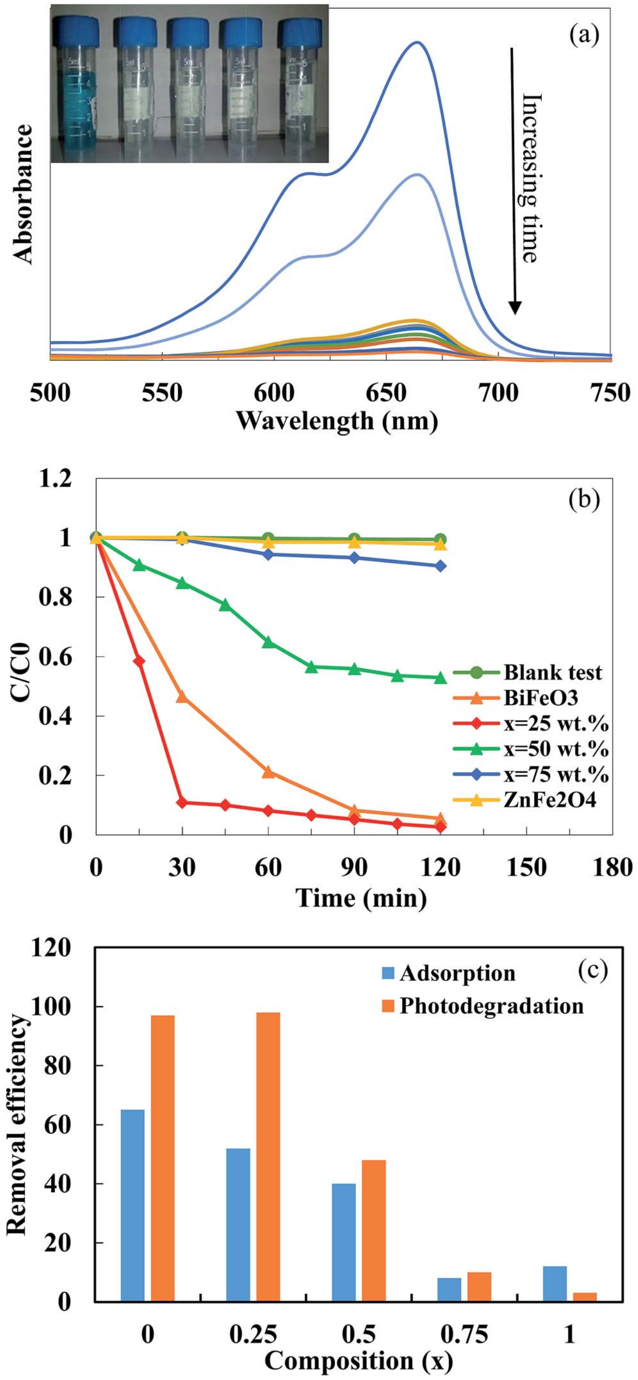

Fig. 7 (a) UV-vis spectra of MB solution in the presence of the $BiFeO_3$-25 wt% $ZnFe_2O_4$ composite (the inset shows the photodegradation of MB), (b) C/C_0 *versus* irradiation time for the photodegradation of MB dye under visible light irradiation by the $BiFeO_3$–$xZnFe_2O_4$ nanocomposites and (c) the removal efficiency of MB dye by adsorption and photodegradation.

on the content of the two components in the composite.[20–22,42] For the optimal content of 25 wt% $ZnFe_2O_4$, the most appropriate $BiFeO_3/ZnFe_2O_4$ heterojunctions might be formed, which benefit the transfer and separation of photogenerated electrons and holes, as can be inferred from the PL spectra.

The suppression of charge recombination in $BiFeO_3$ by pairing with $ZnFe_2O_4$ can be confirmed by photoluminescence (PL) emission spectra, as presented in Fig. 8. As is known, the recombination of excited electrons and holes leads to PL emission, where a lower emission intensity indicates a decrease in recombination probability. Fig. 8 shows the PL emission spectra of the pure $BiFeO_3$ and $BiFeO_3$-25 wt% $ZnFe_2O_4$ photocatalysts at an excitation wavelength of 210 nm. The irradiative recombination process of self-trapped excitations results in an emission band at about 423 nm for pure $BiFeO_3$.[43] Clearly, the PL emission intensity decreases when zinc ferrite was added, which confirms that the coupling of $BiFeO_3$ with $ZnFe_2O_4$ results in an enhanced ability to capture photoinduced electrons in comparison with pure $BiFeO_3$ and pure $ZnFe_2O_4$. The lower PL emission intensity of the $BiFeO_3$-25 wt% $ZnFe_2O_4$ photocatalyst benefits a delay in the recombination rate and, thus, higher photocatalytic activity.[44–47] In addition to the lower recombination rate of electron–hole pairs in the $BiFeO_3$-25 wt% $ZnFe_2O_4$ catalyst, its higher specific surface area can also adsorb more MB dye on the exterior of its particles, as shown in Fig. 7c, hence facilitating the photodegradation of MB dye.

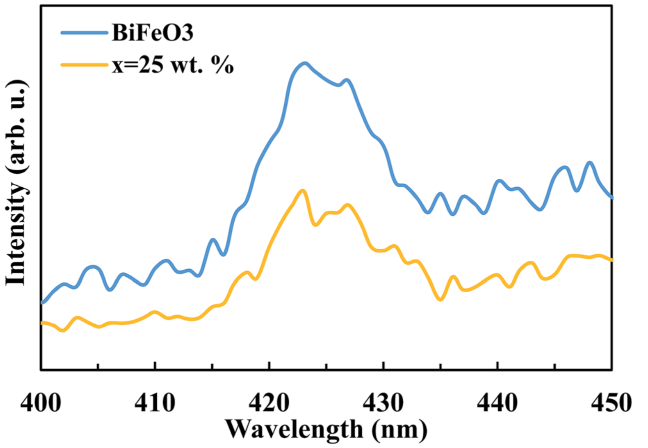

Fig. 8 Comparison of the PL spectra of pure $BiFeO_3$ and $BiFeO_3$-25 wt% $ZnFe_2O_4$ composite.

Based on the above structural characterizations and visible light photocatalytic tests, a possible mechanism for the photodegradation of MB by the $BiFeO_3/ZnFe_2O_4$ photocatalyst under visible light irradiation is proposed. Fig. 9 shows the band positions and transfer path of the photogenerated electron–hole pairs between $BiFeO_3$ and $ZnFe_2O_4$. The conduction (CB) and valence (VB) band positions of $BiFeO_3$ and $ZnFe_2O_4$ at the point of zero charge were obtained from previous reports.[15,48] According to the general p–n heterojunction formation process,[8] the entire energy band of $BiFeO_3$ increases while that of $ZnFe_2O_4$ decreases to achieve an equilibrium state of the Fermi energy level of $BiFeO_3$ and $ZnFe_2O_4$. In this case, the conduction band and valence band of $ZnFe_2O_4$ become higher than that of $BiFeO_3$.

Under visible light irradiation, a high energy photon excites an electron from the valence band (VB) to the conduction band (CB) of $BiFeO_3$ and $ZnFe_2O_4$. The photoinduced electrons in $ZnFe_2O_4$ can easily transfer to $BiFeO_3$, while the holes can transfer to the VB of $ZnFe_2O_4$ from the VB of $BiFeO_3$ conveniently with the help of the internal electric field formed at the interface between $BiFeO_3$ and $ZnFe_2O_4$.[20] Therefore, the photogenerated electrons and holes are efficiently separated between $BiFeO_3$ and $ZnFe_2O_4$ reducing the electron–hole recombination in the composite photocatalyst, thus improving the photo-oxidation efficiency. The separated holes when moving to the surface of the $BiFeO_3/ZnFe_2O_4$ composite could react with H_2O to form hydroxyl radicals, $^{\bullet}OH$, which are powerful oxidative species for the direct oxidation of MB, leading to its decomposition.[49,50] However, the single electron reduction potential of O_2 ($E_0(O_2/O_2^-)$ = −0.046 eV) is less negative than the CB potentials, which confirms that the photoinduced electrons on the surfaces of $BiFeO_3/ZnFe_2O_4$ could not reduce O_2 to yield O_2^- and could not take part in the photodegradation process.[50,51] The suitable $ZnFe_2O_4$ content causes good dispersion in the catalyst, which benefits the formation of heterojunctions between the $BiFeO_3$ and $ZnFe_2O_4$ particles. Therefore, the high separation of charge carriers leads to the high photocatalytic activity of the $BiFeO_3$-25 wt% $ZnFe_2O_4$ photocatalyst.

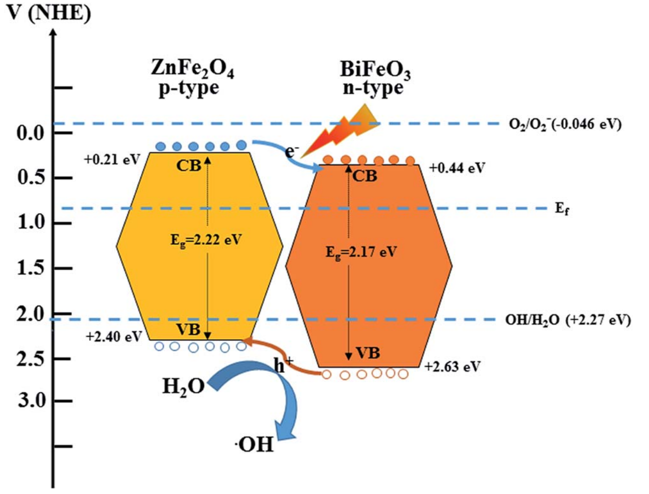

Fig. 9 Schematic for electron–hole transport at the interface of the $BiFeO_3$–$ZnFe_2O_4$ composite.

4. Conclusions

A two-pot approach was used for the synthesis of $BiFeO_3/ZnFe_2O_4$ composites without any impurity species formed between $BiFeO_3$ and $ZnFe_2O_4$. The particle size decreased from 210 nm for pure $BiFeO_3$ to 80 nm for pure $ZnFe_2O_4$. The pure $BiFeO_3$ nanoparticles exhibited a higher specific surface area than the pure $ZnFe_2O_4$ nanoparticles, which may be due to the greater amount of released gaseous products. The magnetization of the $BiFeO_3/ZnFe_2O_4$ composites increased from 0.28 to 1.8 emu g^{-1} with an increase in the $ZnFe_2O_4$ content. The optical band gaps of composites initially decreased from 2.17 to 2.03 eV and then increased to 2.22 eV as a function of the amount of zinc ferrite. The maximum efficiency (∼97%) for the photodegradation of methylene blue under visible light was exhibited for $BiFeO_3$-25 wt% $ZnFe_2O_4$ after 30 minutes irradiation due to the synergic effect between $BiFeO_3$ and $ZnFe_2O_4$.

Conflicts of interest

There are no conflicts to declare.

References

1 E. Casbeer, V. K. Sharma and X.-Z. Li, Synthesis and photocatalytic activity of ferrites under visible light: a review, *Sep. Purif. Technol.*, 2012, **87**, 1–14.

2 Z. Jian, H. Ru and L. Xiaoheng, Efficient visible light driven photocatalytic hydrogen production from water using attapulgite clay sensitized by CdS nanoparticles, *Nanotechnology*, 2013, **24**, 505401.

3 I. Udom, M. K. Ram, E. K. Stefanakos, A. F. Hepp and D. Y. Goswami, One dimensional-ZnO nanostructures: synthesis, properties and environmental applications, *Mater. Sci. Semicond. Process.*, 2013, **16**, 2070–2083.

4 H. Wang, X. Fei, L. Wang, Y. Li, S. Xu, M. Sun, L. Sun, C. Zhang, Y. Li, Q. Yang and Y. Wei, Magnetically separable iron oxide nanostructures-TiO_2 nanofibers hierarchical heterostructures: controlled fabrication and photocatalytic activity, *New J. Chem.*, 2011, **35**, 1795–1802.

5 W. Chen, H. Ruan, Y. Hu, D. Li, Z. Chen, J. Xian, J. Chen, X. Fu, Y. Shao and Y. Zheng, One-step preparation of hollow ZnO core/ZnS shell structures with enhanced photocatalytic properties, *CrystEngComm*, 2012, **14**, 6295–6305.

6 C. M. Raghavan, J. W. Kim, J. Y. Choi, T. K. Song and S. S. Kim, Microstructures and electrical properties of a Li–ZnO/$BiFeO_3$ double-layered thin film fabricated by a chemical solution deposition method, *Ceram. Int.*, 2015, **41**(suppl. 1), S303–S307.

7 J. Hu, Y. Xie, X. Zhou and J. Yang, Solid-state synthesis of ZnO and $ZnFe_2O_4$ to form p–n junction composite in the use of dye sensitized solar cells, *J. Alloys Compd.*, 2016, **676**, 320–325.

8 S. J. A. Moniz, S. A. Shevlin, D. J. Martin, Z.-X. Guo and J. Tang, Visible-light driven heterojunction photocatalysts for water splitting – a critical review, *Energy Environ. Sci.*, 2015, **8**, 731–759.

9 S. Zhang, M. Lu, D. Wu, Y. Chen and N. Ming, Larger polarization and weak ferromagnetism in quenched $BiFeO_3$ ceramics with a distorted rhombohedral crystal structure, *Appl. Phys. Lett.*, 2005, **87**, 262907.

10 J. Kong, Z. Rui, X. Wang, H. Ji and Y. Tong, Visible-light decomposition of gaseous toluene over $BiFeO_3$–$(Bi/Fe)_2O_3$ heterojunctions with enhanced performance, *Chem. Eng. J.*, 2016, **302**, 552–559.

11 T. Choi, S. Lee, Y. Choi, V. Kiryukhin and S.-W. Cheong, Switchable ferroelectric diode and photovoltaic effect in $BiFeO_3$, *Science*, 2009, **324**, 63–66.

12 H. Yi, T. Choi, S. Choi, Y. S. Oh and S. W. Cheong, Mechanism of the switchable photovoltaic effect in ferroelectric $BiFeO_3$, *Adv. Mater.*, 2011, **23**, 3403–3407.

13 S. M. Masoudpanah, S. M. Mirkazemi, R. Bagheriyeh, F. Jabbari and F. Bayat, Structural, magnetic and photocatalytic characterization of $Bi_{1-x}La_xFeO_3$ nanoparticles synthesized by thermal decomposition method, *Bull. Mater. Sci.*, 2017, **40**, 93–100.

14 T. Soltani and M. H. Entezari, Photolysis and photocatalysis of methylene blue by ferrite bismuth nanoparticles under sunlight irradiation, *J. Mol. Catal. A: Chem.*, 2013, **377**, 197–203.

15 S.-M. Lam, J.-C. Sin and A. R. Mohamed, A newly emerging visible light-responsive $BiFeO_3$ perovskite for photocatalytic applications: a mini review, *Mater. Res. Bull.*, 2017, **90**, 15–30.

16 Z. Li, Y. Shen, Y. Guan, Y. Hu, Y. Lin and C.-W. Nan, Bandgap engineering and enhanced interface coupling of graphene–$BiFeO_3$ nanocomposites as efficient photocatalysts under visible light, *J. Mater. Chem. A*, 2014, **2**, 1967–1973.

17 T. Soltani and M. H. Entezari, Solar photocatalytic degradation of RB5 by ferrite bismuth nanoparticles synthesized *via* ultrasound, *Ultrason. Sonochem.*, 2013, **20**, 1245–1253.

18 S. M. Masoudpanah, S. M. Mirkazemi, S. Shabani and P. T. Dolat Abadi, The effect of the ethylene glycol to metal nitrate molar ratio on the phase evolution, morphology and magnetic properties of single phase $BiFeO_3$ nanoparticles, *Ceram. Int.*, 2015, **41**, 9642–9646.

19 P. Reddy Vanga, R. V. Mangalaraja and M. Ashok, Structural, magnetic and photocatalytic properties of La and alkaline co-doped $BiFeO_3$ nanoparticles, *Mater. Sci. Semicond. Process.*, 2015, **40**, 796–802.

20 T. Fan, C. Chen and Z. Tang, Hydrothermal synthesis of novel $BiFeO_3$/$BiVO_4$ heterojunctions with enhanced photocatalytic activities under visible light irradiation, *RSC Adv.*, 2016, **6**, 9994–10000.

21 F. Niu, D. Chen, L. Qin, N. Zhang, J. Wang, Z. Chen and Y. Huang, Facile Synthesis of Highly Efficient p–n Heterojunction CuO/$BiFeO_3$ Composite Photocatalysts with Enhanced Visible-Light Photocatalytic Activity, *ChemCatChem*, 2015, **7**, 3279–3289.

22 X. Wang, W. Mao, J. Zhang, Y. Han, C. Quan, Q. Zhang, T. Yang, J. Yang, X. A. Li and W. Huang, Facile fabrication of highly efficient g-C_3N_4/$BiFeO_3$ nanocomposites with enhanced visible light photocatalytic activities, *J. Colloid Interface Sci.*, 2015, **448**, 17–23.

23 T. Soltani and B.-K. Lee, Sono-synthesis of nanocrystallized $BiFeO_3$/reduced graphene oxide composites for visible photocatalytic degradation improvement of bisphenol A, *Chem. Eng. J.*, 2016, **306**, 204–213.

24 F. Chen, W. An, L. Liu, Y. Liang and W. Cui, Highly efficient removal of bisphenol A by a three-dimensional graphene hydrogel-AgBr@rGO exhibiting adsorption/photocatalysis synergy, *Appl. Catal., B*, 2017, **217**, 65–80.

25 X. Wang, Y. Liang, W. An, J. Hu, Y. Zhu and W. Cui, Removal of chromium(VI) by a self-regenerating and metal free g-C_3N_4/graphene hydrogel system *via* the synergy of adsorption and photo-catalysis under visible light, *Appl. Catal., B*, 2017, **219**, 53–62.

26 Y. Li, W. Cui, L. Liu, R. Zong, W. Yao, Y. Liang and Y. Zhu, Removal of Cr(VI) by 3D TiO_2-graphene hydrogel *via* adsorption enriched with photocatalytic reduction, *Appl. Catal., B*, 2016, **199**, 412–423.

27 L. Liu, Y. Qi, J. Lu, S. Lin, W. An, Y. Liang and W. Cui, A stable Ag_3PO_4@g-C_3N_4 hybrid core@shell composite with enhanced visible light photocatalytic degradation, *Appl. Catal., B*, 2016, **183**, 133–141.

28 S. M. Masoudpanah, M. Hasheminisari and A. Ghasemi, Magnetic properties and photocatalytic activity of $ZnFe_{2-x}La_xO_4$ nanoparticles synthesized by sol–gel autocombustion method, *J. Sol-Gel Sci. Technol.*, 2016, **80**, 487–494.

29 P. Uniyal and K. L. Yadav, Observation of the room temperature magnetoelectric effect in Dy doped $BiFeO_3$, *J. Phys.: Condens. Matter*, 2009, **21**, 012205.

30 S. Shabani, S. M. Mirkazemi, S. M. Masoudpanah and P. T. Dolat Abadi, Synthesis and Characterization of Pure Single Phase $BiFeO_3$ Nanoparticles by the Glyoxylate Precursor Method, *J. Supercond. Novel Magn.*, 2014, **27**, 2795–2801.

31 T. Gao, Z. Chen, Y. Zhu, F. Niu, Q. Huang, L. Qin, X. Sun and Y. Huang, Synthesis of $BiFeO_3$ nanoparticles for the visible-light induced photocatalytic property, *Mater. Res. Bull.*, 2014, **59**, 6–12.

32 M. Tyagi, M. Kumari, R. Chatterjee and P. Sharma, Raman scattering spectra, magnetic and ferroelectric properties of $BiFeO_3$–$CoFe_2O_4$ nanocomposite thin films structure, *Phys. B*, 2014, **448**, 128–131.

33 Z. Wang, D. Schiferl, Y. Zhao and H. S. C. O'Neill, High pressure Raman spectroscopy of spinel-type ferrite $ZnFe_2O_4$, *J. Phys. Chem. Solids*, 2003, **64**, 2517–2523.

34 K. S. W. Sing, D. H. Everett, R. A. W. Haul, L. Moscou, R. A. Pierotti, J. Rouquerol and T. Siemieniewska, Reporting Physisorption Data for Gas/Solid Systems, *Handbook of Heterogeneous Catalysis*, Wiley-VCH Verlag GmbH & Co. KGaA, 2008.

35 B. Pourgolmohammad, S. M. Masoudpanah and M. R. Aboutalebi, Synthesis of $CoFe_2O_4$ powders with high surface area by solution combustion method: effect of fuel content and cobalt precursor, *Ceram. Int.*, 2017, **43**, 3797–3803.

36 T.-J. Park, G. C. Papaefthymiou, A. J. Viescas, A. R. Moodenbaugh and S. S. Wong, Size-Dependent Magnetic Properties of Single-Crystalline Multiferroic $BiFeO_3$ Nanoparticles, *Nano Lett.*, 2007, **7**, 766–772.

37 V. Blanco-Gutierrez, E. Climent-Pascual, M. J. Torralvo-Fernandez, R. Saez-Puche and M. T. Fernandez-Diaz, Neutron diffraction study and superparamagnetic behavior of $ZnFe_2O_4$ nanoparticles obtained with different conditions, *J. Solid State Chem.*, 2011, **184**, 1608–1613.

38 M. A. Butler, Photoelectrolysis and physical properties of the semiconducting electrode WO_2 , *J. Appl. Phys.*, 1977, **48**, 1914–1920.

39 H. Wang, Y. Zheng, M.-Q. Cai, H. Huang and H. L. W. Chan, First-principles study on the electronic and optical properties of $BiFeO_3$, *Solid State Commun.*, 2009, **149**, 641–644.

40 J. Feng, L. Su, Y. Ma, C. Ren, Q. Guo and X. Chen, $CuFe_2O_4$ magnetic nanoparticles: a simple and efficient catalyst for the reduction of nitrophenol, *Chem. Eng. J.*, 2013, **221**, 16–24.

41 J. Li, Z. Liu and Z. Zhu, Magnetically separable $ZnFe_2O_4$, Fe_2O_3/$ZnFe_2O_4$ and ZnO/$ZnFe_2O_4$ hollow nanospheres with enhanced visible photocatalytic properties, *RSC Adv.*, 2014, **4**, 51302–51308.

42 L. Zhang, Y. He, P. Ye, Y. Wu and T. Wu, Visible light photocatalytic activities of $ZnFe_2O_4$ loaded by Ag_3VO_4 heterojunction composites, *J. Alloys Compd.*, 2013, **549**, 105–113.

43 Y. Chen, Y. Tang, S. Luo, C. Liu and Y. Li, TiO_2 nanotube arrays co-loaded with Au nanoparticles and reduced graphene oxide: facile synthesis and promising photocatalytic application, *J. Alloys Compd.*, 2013, **578**, 242–248.

44 Y. Liang, S. Lin, L. Liu, J. Hu and W. Cui, Oil-in-water self-assembled Ag@AgCl QDs sensitized Bi_2WO_6: enhanced photocatalytic degradation under visible light irradiation, *Appl. Catal., B*, 2015, **164**, 192–203.

45 Y. Zhang, W. Cui, W. An, L. Liu, Y. Liang and Y. Zhu, Combination of photoelectrocatalysis and adsorption for removal of bisphenol A over TiO_2-graphene hydrogel with 3D network structure, *Appl. Catal., B*, 2018, **221**, 36–46.

46 H. Wang, Y. Liang, L. Liu, J. Hu and W. Cui, Highly ordered TiO_2 nanotube arrays wrapped with g-C_3N_4 nanoparticles for efficient charge separation and increased photoelectrocatalytic degradation of phenol, *J. Hazard. Mater.*, 2018, **344**, 369–380.

47 H. Wang, Y. Liang, L. Liu, J. Hu and W. Cui, Reduced graphene oxide wrapped Bi_2WO_6 hybrid with ultrafast charge separation and improved photoelectrocatalytic performance, *Appl. Surf. Sci.*, 2017, **392**, 51–60.

48 J. He, R. Guo, L. Fang, W. Dong, F. Zheng and M. Shen, Characterization and visible light photocatalytic mechanism of size-controlled $BiFeO_3$ nanoparticles, *Mater. Res. Bull.*, 2013, **48**, 3017–3024.

49 H. Cheng, B. Huang, Y. Dai, X. Qin and X. Zhang, One-Step Synthesis of the Nanostructured AgI/BiOI Composites with Highly Enhanced Visible-Light Photocatalytic Performances, *Langmuir*, 2010, **26**, 6618–6624.

50 D. Wang, T. Kako and J. Ye, Efficient Photocatalytic Decomposition of Acetaldehyde over a Solid-Solution Perovskite $(Ag_{0.75}Sr_{0.25})(Nb_{0.75}Ti_{0.25})O_3$ under Visible-Light Irradiation, *J. Am. Chem. Soc.*, 2008, **130**, 2724–2725.

51 L. Liu, L. Ding, Y. Liu, W. An, S. Lin, Y. Liang and W. Cui, A stable Ag_3PO_4@PANI core@shell hybrid: enrichment photocatalytic degradation with π–π conjugation, *Appl. Catal., B*, 2017, **201**, 92–104.